Microscopy and Microanalysis (2018), **24**, 249–255
doi:10.1017/S1431927618000223

Microscopy AND Microanalysis

Original Article

Electron Source Brightness and Illumination Semi-Angle Distribution Measurement in a Transmission Electron Microscope

Felix Börrnert, Julian Renner and Ute Kaiser
Materialwissenschaftliche Elektronenmikroskopie, Universität Ulm, Albert-Einstein-Allee 11, 89081 Ulm, Germany

Abstract

The electron source brightness is an important parameter of an electron microscope. Reliable and easy brightness measurement routes are not easily found. A determination method for the illumination semi-angle distribution in transmission electron microscopy is even less well documented. Herein, we report a facile measurement route for both entities and demonstrate it on a state-of-the-art instrument. The reduced axial brightness of the FEI X-FEG with a monochromator was determined to be larger than 10^8 A/(m^2 sr V).

Key words: TEM, electron source, brightness, optical parameters, electron microscopy

(Received 18 September 2017; revised 8 March 2018; accepted 27 March 2018)

Introduction

The brightness of the electron source is one of the central parameters governing the performance of an electron microscope. It is a major factor for the practically reachable resolution, not only in scanning transmission electron microscopy (STEM), but also in conventional transmission electron microscopy (TEM). In STEM, the source brightness dictates the current in the electron probe for a given probe diameter. While in theory, one can make the probe diameter infinitely small, this does not work in reality since there is no signal left without a significant electron current in the probe. The introduction of aberration correction into STEM effectively did not improve the ultimate resolving power of the instruments but rather the usable signal for a given resolution (Müller et al., 2006). Also in TEM, the image's signal-to-noise ratio and ultimately its resolution is a function of the total dose in the image. In practice, the acquisition time often is limited due to sample drift, vibration, and damage, and therefore, a high dose rate is needed. Although the dose rate seems to be more related to the total current coming from the source, the brightness additionally includes the illumination semi-angle distribution.

In TEM information transfer, the illumination semi-angle distribution dominates the information dampening for the nonaberration-corrected case (Erni, 2010). Here, knowledge of the semi-angle distribution is needed for quantitative contrast evaluation. This value is also crucial in off-axis electron holography because there it governs the interference fringe contrast and thus the achievable information content (Lichte et al., 2013; Röder et al., 2014).

Generally, in the literature, we find the terminus illumination semi-angle α which, in fact, is not a single angle but an angle distribution. Since the smallest possible illumination semi-angle distribution is linked to the spatial electron source emission profile by a Fourier transform, we approximate the spatial electron source emission profile to be Gaussian (van Veen et al., 2001) and thus, we automatically assume the illumination semi-angle distribution to be Gaussian as well, and therefore describe it with the help of its standard deviation σ_α.

The assessment of the illumination semi-angle distribution cannot be found in textbooks. For partial spatial coherence dampening envelopes in TEM, the illumination semi-angle distribution is usually given or assumed. Although there is pioneering work by Joachim Frank from the 1970s and Tsuji and St. John Manley in the 1980s (Frank, 1976; Tsuji & St. John Manley, 1983), the illumination semi-angle distribution is derived from the brightness given for the electron source and the dose in an image in most cases. A more or less direct method to measure the illumination semi-angle distribution is the determination of the diffraction spots' minimal size (Hosokawa et al., 1991); unfortunately, for modern high-brightness electron sources, this method over-estimates the illumination semi-angle distribution due to its small value in combination with a limited projective/camera resolution. At least, in off-axis electron holography, one can obtain it by the bi-prism voltage-dependent hologram fringe contrast. Unfortunately, the illumination semi-angle distribution changes with magnification and illumination density. Therefore, a realistic value must be obtained for the respective image acquisition conditions.

Here, we demonstrate a facile and straightforward way to measure the illumination semi-angle distribution in TEM and subsequently the electron source brightness via a simple defocus series of Young's fringes tests. The experiments demonstrated here were performed on a chromatic- and geometric-aberration-corrected microscope (Linck et al., 2016). Nevertheless, this method works on any transmission electron microscope. An aberration corrector just adds the convenience of out-of-the-box automated defocus measurement and automated optical image shift. Additionally, the aberration-corrected case demonstrates the

Author for correspondence: Felix Börrnert, E-mail: felix.boerrnert@uni-ulm.de
Cite this article: Börrnert F, Renner J, Kaiser U (2018) Electron Source Brightness and Illumination Semi-Angle Distribution Measurement in a Transmission Electron Microscope. *Microsc Microanal* **24**(3): 249–255. doi: 10.1017/S1431927618000223

© Microscopy Society of America 2018

Downloaded from https://www.cambridge.org/core. Ulm University, on 16 Jan 2019 at 15:38:26, subject to the Cambridge Core terms of use, available at https://www.cambridge.org/core/terms. https://doi.org/10.1017/S1431927618000223

effectiveness of the method even when the illumination dampening effect is superposed by dominating other dampening effects and also shows the importance of taking the other dampening mechanisms into account.

The Illumination Semi-Angle Distribution

The ideal TEM illumination is a plane wave incident to the sample plane. This corresponds to perfectly parallel electron trajectories in the illuminating electron beam. Here, one has to distinguish between the conventional parallel or isoplanatic illumination (Köhler illumination) and a finite illumination semi-angle distribution stemming from the limited axial brightness of the electron source.

An isoplanatic illumination means that the illumination direction is independent of the position in the sample plane and could be achieved with a proper layout of the condenser system of a microscope. Unfortunately, in practice, either a telescopic condenser lens doublet is missing to provide parallel illumination at various current densities in the sample plane or the alignment possibilities of this doublet are not optimal due to missing tilt/shift deflector pairs; thus, it is a technical issue.

Independent of the non-isoplanatic illumination, the reason for the finite illumination semi-angle distribution is the finite size of the virtual electron source. The illumination is, one can say, the back focal plane of the source's image and thus the Fourier transform of the virtual electron source. For a perfect plane wave illumination one would need a perfect point source. While in theory, this is easily doable by demagnifying the source optically, the electron current that is left for imaging also approaches zero due to the inherently limited axial brightness of the electron source. Apart from the emission process in the physical electron source itself, effects like, for example, the Löffler effect (Löffler, 1964) (often incorrectly called the lateral Boersch effect[a]) and ultimately the nature of the electrons being Fermions prohibit an arbitrary enhancement of the axial brightness of the virtual electron source fundamentally.

What is the influence of a finite illumination semi-angle distribution? It may be twofold: First, the sample exit-plane wave is the sum of projections from different directions. But here, if one assumes a semi-angle of even 1 mrad, for a target resolution of 1 Å, by simple geometric reasoning the sample thickness must be larger than 50 nm to show any effect. We will see that 1 mrad would be a very large semi-angle and with 50 nm sample thickness, other factors limit the achievable resolution. Second, the dominant mechanism is that a tilt in the sample plane results in a shift in the back focal plane and thus, the different incoming waves sample the geometrical aberration induced virtual phase plate at different positions as sketched in Figure 1. Consequently, the gradient of this virtual phase plate generates a blurring of the image points, an effect of the so-called illumination dampening envelope function (Erni, 2010).

In the following discussions, the description of the information transfer stays within the framework of linear imaging. Generally, this assumption is a good approximation for thin samples and not too heavy elements at medium electron acceleration voltages. The impact of nonlinear information transfer is discussed briefly later.

[a]Both the Boersch effect and the Löffler effect are electron–electron interactions; the former smears out the energy distribution of the electrons in the beam, the latter enlarges their spatial distribution.

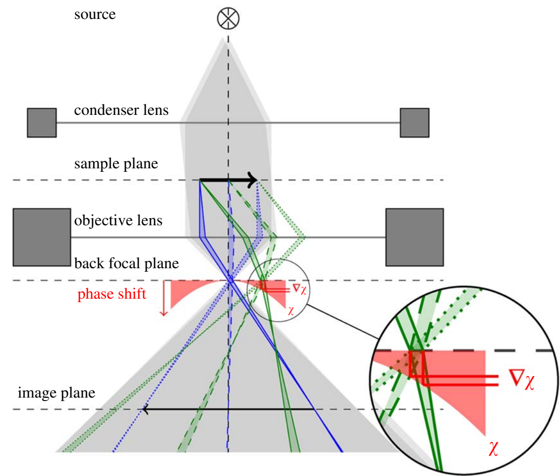

Fig. 1. Scheme for the illumination dampening mechanism. The gray background stands for a parallel illumination originating from two discrete source points and thus showing an angular distribution with just one discrete angle. The blue rays symbolize the forward scattered electron beams that pass the objective lens' back focal plane near the optic axis. The green rays represent a set of beams all scattered with the same larger angle and therefore passing the back focal plane away from the optic axis. The red shaded area symbolizes the virtual phase plate χ due to the geometric aberrations. In real space, it is infinitely thin in the back focal plane. The collective shift of the green rays in the image plane represents the contrast delocalization and the broadening of each single beam in the image plane is the contrast dampening.

The isotropic illumination dampening envelope function has the form

$$E_{\mathrm{illu}}(q) = \mathrm{e}^{-\frac{2\pi^2}{\lambda^2}\sigma_\alpha^2(\nabla\chi)^2}, \tag{1}$$

with the electron wavelength λ, the illumination semi-angle distribution σ_α, and the gradient of the aberration function

$$\nabla\chi = C_1(\lambda q) + C_3(\lambda q)^3 + C_5(\lambda q)^5 + \ \ldots$$

Here, only the axially isotropic aberrations are taken into account, which is reasonable for any well-aligned microscope. C_i are the spherical aberration coefficients of the different orders, with $i = 1$ representing the defocus.

The illumination semi-angle distribution is the only unknown parameter here since the aberrations are either known or can be determined with the help of a Zemlin tableau. Unfortunately, the illumination dampening is not the only information dampening mechanism. There is also the focus spread dampening and—only in a chromatically corrected microscope—the image spread (Uhlemann et al., 2013). Again, both are assumed to be isotropic in this case. All other information dampening mechanisms can be safely neglected here. Since both the focus spread dampening envelope function,

$$E_{\mathrm{fs}}(q) = \mathrm{e}^{-\frac{\pi^2}{2\lambda^2}\sigma_{\mathrm{fs}}^2(\lambda q)^4}, \tag{2}$$

with the focus spread σ_{fs}, and the image spread dampening envelope function,

$$E_{\mathrm{is}}(q) = \mathrm{e}^{-\frac{2\pi^2}{\lambda^2}\sigma_{\mathrm{is}}^2(\lambda q)^2}, \tag{3}$$

with the image spread σ_{is}, show a comparably small gradient in q, they do influence the total dampening considerably even if the much steeper illumination dampening envelope function dominates the information limit.

Downloaded from https://www.cambridge.org/core. Ulm University, on 16 Jan 2019 at 15:38:26, subject to the Cambridge Core terms of use, available at https://www.cambridge.org/core/terms.
https://doi.org/10.1017/S1431927618000223

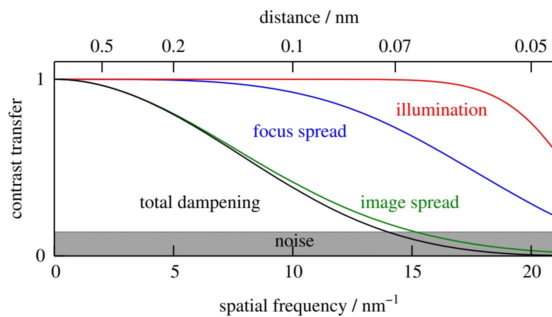

Fig. 2. Total contrast dampening envelope function of the SALVE instrument with its constituents. The parameters used are $U = 80\,\mathrm{kV}$ and $\alpha = 0.07\,\mathrm{mrad}$. Lentzen conditions are employed with a $C_5 = 3\,\mathrm{mm}$. The focus spread $\sigma_{\mathrm{fs}} = 0.29\,\mathrm{nm}$ and the image spread $\sigma_{\mathrm{is}} = 0.021\,\mathrm{nm}$.

Finally, the total dampening envelope is the product of all dampening envelopes of the different origins (Erni, 2010),

$$E_{\mathrm{total}}(q) = \prod_m E_m(q),$$

where m in this case stands for illu, fs, and is.

As an example, Figure 2 illustrates the different dampening envelope functions and the total dampening for the SALVE instrument at 80 kV (Linck et al., 2016). The information limit is the point where the total dampening envelope function enters the noise level indicated in gray in the plot. The noise level is conventionally assumed as e^{-2} of the total contrast (Erni, 2010). This convention is still meaningful because the noise is dominated by the Poisson noise of the imaging electrons themselves, and thus, the noise level is mainly dependent on the total electron dose in the image regardless of the detector. The mean total dose per resolved image point in high-resolution imaging remained nearly constant over the years as it is a compromise between a sufficiently low noise level and a reasonable image acquisition time, because longer acquisition times are inherently linked with any sort of drift effects and sample alteration due to beam interaction. Nevertheless, when the total dose in the image is very small or the background noise from the sample (e.g. from an amorphous support layer) is large, the signal-to-noise ratio can drop substantially and the noise level has to be shifted to larger values.

To be consistent, we use the standard deviation for all distributions σ_α, σ_{fs}, and σ_{is} as a convention. Often, one finds the use of the full width at half maximum (FWHM), where one needs to apply a factor like $\alpha_{\mathrm{FWHM}} = 2\sqrt{2\ln 2}\,\sigma_\alpha \approx 2.35\,\sigma_\alpha$.

To measure the illumination semi-angle distribution under a certain illumination condition, we determine the information limit with the help of a Young's fringes test at different defoci. For the Young's fringes test, one superposes two micrographs of a thin amorphous specimen slightly shifted by $\Delta x = (\Delta q)^{-1}$ and Fourier transforms the sum. Due to the shift, a modulation $(1 + \cos\Delta q)$ is introduced into the diffractogram intensity (Zemlin & Schiske, 1980). In the diffractogram, one then can determine the extent of the modulated signal in q and thus determine the information limit. When using the Young's fringes test, it is known that nonlinear information transfer can falsify the information transfer measurement (Barthel & Thust, 2008). The best way to prevent this is to use a suitable test sample. Nevertheless, we will see below that nonlinear information transfer in this case does not affect the correct determination of the illumination semi-angle distribution.

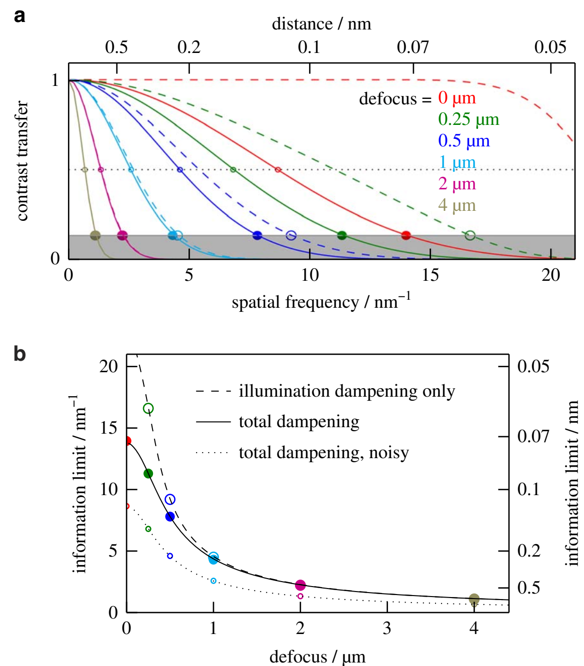

Fig. 3. Illumination semi-angle measurement principle via an information limit determination in a defocus series. **a:** Total contrast dampening envelope function (solid lines) and illumination dampening function (dashed lines) for different defoci. The gray region is the conventional noise level and the dotted line exemplifies a case of a very noisy image. The different defoci are color coded and indicated in the plot. The respective information limits are indicated by the color-coded circles. **b:** Defocus-dependent information limit for the three cases with the same color and line coding. The parameters used are the same as in Figure 2.

Figure 3 demonstrates the working principle of the measurement. The top panel (Fig. 3a) plots show the dampening envelope functions with the corresponding information limit (*circles*) for a series of defoci. The defoci are color coded and their values written in the plot area. Additionally, three cases are shown: the solid lines represent the total dampening envelope functions and the dashed lines solely the illumination dampening function, neglecting focus spread and image spread. The deviation between these two is rather striking, even at relatively large defoci of about $0.5\,\mu\mathrm{m}$ when the illumination dampening becomes largely dominant. Additionally, the dotted line indicates an increased noise level, with the small circles pointing out the respective information limits, clarifying the reason for a much reduced information limit at low signal-to-noise ratio in the image.

The bottom panel (Fig. 3b) plots directly the defocus dependence of the information limit for the three cases. The color and line coding are the same as above. Again, the deviation between the total dampening and the illumination dampening only up to relatively large defoci is substantial. At very large defoci from $1\,\mu\mathrm{m}$ upwards, the change in the information limit becomes small with the chosen illumination angle distribution, therefore, the measurement error in the Young's fringes test would have a serious impact on the illumination semi-angle distribution error if one solely took these large defoci into account. Thus, a single measurement of the information limit is not sufficient to determine the illumination semi-angle distribution, neither at small defocus where the influence of focus spread and possibly image spread masks the effects of the illumination semi-angle distribution nor at large defocus where the illumination dampening is

Downloaded from https://www.cambridge.org/core. Ulm University, on 16 Jan 2019 at 15:38:26, subject to the Cambridge Core terms of use, available at https://www.cambridge.org/core/terms.
https://doi.org/10.1017/S1431927618000223

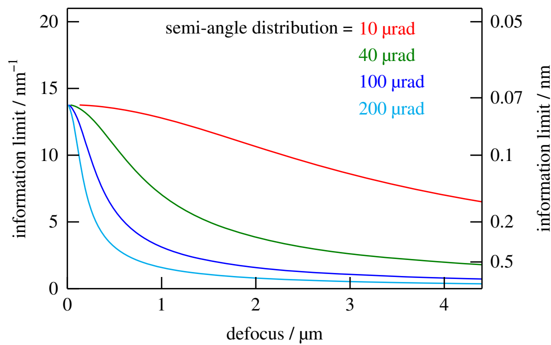

Fig. 4. Defocus-dependent information limit calculated for different illumination semi-angle distributions. The parameters used besides the illumination semi-angle distribution are the same as in Figure 2.

dominating the information limit, but the error is large due to the flatness of the curve.

Sometimes, only the defocus is taken into account in the illumination dampening envelope function. Ignoring the higher-order geometric aberrations makes this function diverge when approaching zero defocus, with, according to our calculations, significant deviations below 250 nm defocus for our 80 kV settings. Likewise, for a 300 kV third-order spherical-aberration-corrected microscope, the discrepancy is significant below 120 nm defocus. Nevertheless, if one also applies the other dampening envelopes, as one has to in the case of aberration-corrected microscopes, the deviations are marginal. However, in the case of most uncorrected microscopes, the illumination dampening dominates the information limit and we observe huge deviations below 1 μm defocus, if one neglects the higher-order spherical aberrations in the calculations.

As a remark, in this case the defoci are indeed positive since we use a negative third-order spherical aberration to counter-balance the finite positive fifth order spherical aberration. Of course, the experiment is also valid for negative defoci but one has to care about the sign of the third-order spherical aberration.

Figure 4 demonstrates the behavior of the defocus-dependent information limit for varying illumination semi-angle distribution values. The prominent change of the curve's shape makes the systematic error of the final fit of the measured values small. This is, of course, only valid if one samples the curve over a sufficiently large range of defoci.

As can be seen in the 10-μrad plot, the information limit is much less affected even for several micrometers of defocus. As mentioned above, it is possible to install very small illumination semi-angle distributions, but at the expense of electron dose rate because of the electron source's finite brightness. This is used for example in imaging biological samples at large defoci. There, the large defocus is needed for inducing sufficient contrast and a small dose rate facilitates low total doses per specimen area, while the resulting small illumination semi-angle distribution does not lower the information limit too much (Tiemeijer et al., 2012*a*).

The Electron Source Brightness

With the proper illumination semi-angle distribution measured, the electron source brightness is easily determined from the same experimental images if the camera's conversion rate is known.

The reduced axial brightness is defined as (Reimer & Kohl, 2008)

$$B_r = \frac{j}{\Delta\Omega\ U^*}, \tag{4}$$

with the mean electron current density $j = \frac{\Delta I}{\Delta A}$, the solid angle $\Delta\Omega$, and the relativistically modified electron acceleration voltage U^*. We use the reduced axial brightness because it is an intrinsic property of the electron source and thus independent of the acceleration voltage. In the literature, the brightness $B = B_r U^*$ is usually given as a numerical value that obviously is more than five orders of magnitude larger for medium voltage electron microscopes, but always has to be stated and scaled with the corresponding electron acceleration voltage.

The solid angle is linked with the semi-angle via the relation,

$$\Omega = 4\pi \sin^2\frac{\alpha}{2} \approx \pi\alpha^2.$$

Since we do not deal with the illumination semi-angle but with its Gaussian distribution, we use $\Delta\Omega \approx \pi\sigma_\alpha^2$.

The mean current density can easily be determined from the original micrograph of a Young's fringes test. Here, the camera's magnification table and conversion rate should be well calibrated.

Due to the reduced axial brightness being constant, one can use the simple relation:

$$\sigma_\alpha^2 = \frac{j}{\pi B_r U^*} \tag{5}$$

to estimate, from the micrograph, the illumination semi-angle distribution for a certain illumination setup after changing the illumination current density.

Experimental

The investigations were performed with the SALVE (Sub-Ångström Low-Voltage Electron microscopy) instrument (Linck et al., 2016). This is a dedicated low-voltage microscope (20–80 kV) based on a FEI Titan Themis[3] 60–300 transmission electron microscope (FEI Electron Optics B.V., Eindhoven, The Netherlands) and fitted with the CEOS SALVE aberration corrector (CEOS GmbH, Heidelberg, Germany), that corrects axial geometrical aberrations up to the fifth order, off-axial geometrical aberrations up to the third order, and the first-order chromatic aberrations. The camera used is a FEI CETA 16 M fiber coupled CMOS camera. The instrument's electron source is a FEI X-FEG Schottky type with a single Wien filter type monochromator that was switched off.

The image acquisition time was 2 s for the high dose rate Young's fringes tests and 10 s for the low dose rate ones. High dose rate illumination means, we condense the illuminating electron beam in a way that the illuminated spot in the sample plane is slightly larger than the area imaged by the camera. Additionally, we chose electron source/monochromator settings in which a maximum number of electrons provided by the source also contribute to the illuminating beam. On the other hand, the low dose rate conditions were installed by defocusing the monochromator focus until the dose rate measured in the image is ~30 $e^-/(\text{Å}^2$ s), a value typically used in imaging biological samples.

The respective magnification was chosen in a way that the maximum information is over-sampled at least four times by the camera to avoid any additional influences of the camera's modulation transfer function on the measurement. The image shift for

Downloaded from https://www.cambridge.org/core. Ulm University, on 16 Jan 2019 at 15:38:26, subject to the Cambridge Core terms of use, available at https://www.cambridge.org/core/terms.
https://doi.org/10.1017/S1431927618000223

the Young's fringes test was done by the corrector's image shift wobbler. The defocus values were set by moving the sample along the optical axis with the sample stage's piezoelectric drives and controlling every single defocus value with the help of the defocus measurement routine of the corrector software.

The camera's electron conversion rates for the different electron energies were calibrated with the help of a home-built Faraday cup at the sample position and the magnification calibration was done by imaging a graphene sample.

When defocusing strongly, even by moving the sample along the optic axis, the magnification changes. Additionally, the measurement of the defocus by the corrector software depends on the magnification calibration. The actual magnification change is linearly dependent on the defocus, while the defocus measurement has a quadratic dependency on the magnification calibration. We measured the apparent magnification change with defocus with the help of a standard gold poly-crystalline sample at the relevant magnifications and in the defocus range of 0–500 nm (80 kV) and 0–4 μm (20 kV), respectively. We used gold instead of graphene (that we used for the magnification calibration) because only gold gave a usable signal over the whole defocus range. The magnification variation was less than 3% and thus sufficiently small to be neglected.

The sample used for the Young's fringes test was 1.5 nm thick amorphous tungsten.

Exemplary Measurement

Figure 5 show exemplarily parts of a series of Young's fringes tests at different defoci for a high dose rate illumination at 80 kV electron acceleration voltage.

The Young's fringes tests were performed by taking a micrograph of thin amorphous tungsten while shifting the image and subsequently Fourier transforming the micrograph. In addition, the tests were performed for two orthogonal shifting directions, both shown in Figure 5 for every defocus. This helps to evaluate possible non-isotropies in the signal transfer. The depicted Fourier transforms of the image are cropped with a factor of two, thus the sampling is more than five pixels per theoretically resolved point, making the modulation transfer function of the camera negligible for the measurement. Any residual dampening effect due to the camera's modulation transfer function would act like an additional image spread and is thus taken care of by the image spread dampening envelope function.

The substantial decay of the information limit with increasing defocus can be readily seen. Also, that the assessment of the information limit when it is small bears a large relative error, because of the small ratio between the fringe disk radius and the radius uncertainty. The respective information limit value we set to the ultimate visibility limit of the fringe signal.

The evaluation of the different focus series is presented in Figure 6. The filled circles represent the measured information limits for high dose rate illumination conditions, while the empty circles represent the measured information limits for low dose rate illumination conditions. The measurements at 20 kV electron acceleration voltage are indicated in green while those at 80 kV are in red. To extract the desired illumination semi-angle distribution σ_α, we determine where the product of equations (1), (2), and (3) crosses the noise level

$$\frac{1}{e^{2N}} = e^{-\frac{2\pi^2}{\lambda^2}\sigma_\alpha^2\left(C_1(\lambda q)+C_3(\lambda q)^3+C_5(\lambda q)^5\right)^2} \cdot e^{-\frac{\pi^2}{2\lambda^2}\sigma_{\mathrm{fs}}^2(\lambda q)^4} \cdot e^{-\frac{2\pi^2}{\lambda^2}\sigma_{\mathrm{is}}^2(\lambda q)^2}$$

and resolve it for the defocus C_1. Conventionally, one would try to solve it for the information limit spatial frequency q since we measure q and control C_1 but the result would be a cumbersome tenth order polynomial. Thus, the lines in Figure 6 are fits of the function,

$$C_1 = \frac{\sqrt{N\frac{\lambda^2}{\pi^2} - \sigma_{\mathrm{is}}^2(\lambda q)^2 - \frac{1}{4}\sigma_{\mathrm{fs}}^2(\lambda q)^4}}{\sigma_\alpha(\lambda q)} - C_3(\lambda q)^2 - C_5(\lambda q)^4,$$

where the only variable parameters are the illumination semi-angle distribution σ_α and the signal-to-noise ratio factor N. For the conventional noise level of e^{-2} contrast, that we normally use, the signal-to-noise ratio factor is unity ($N=1$) and indeed, for the high dose rate illumination this value fits well, while for the low dose rate

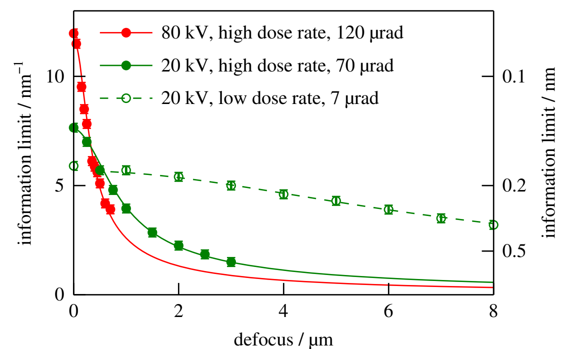

Fig. 6. Illumination semi-angle assessment for different electron acceleration voltages and different dose rate illumination.

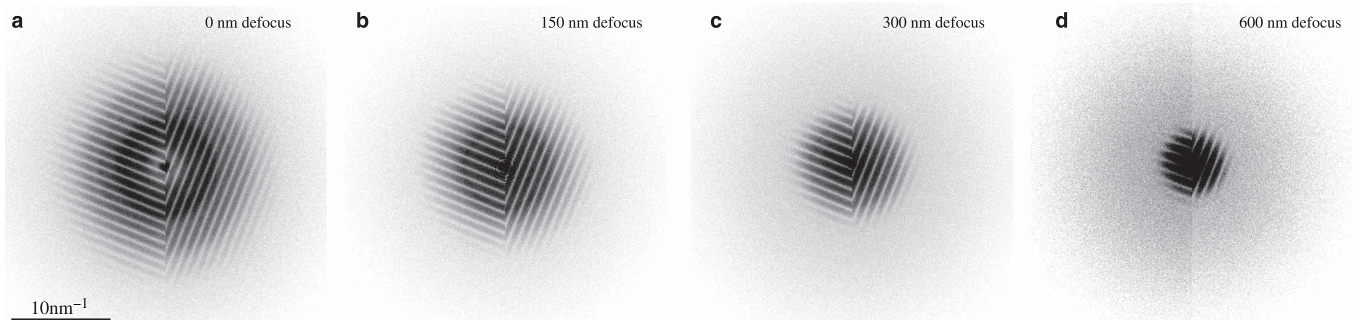

Fig. 5. Series of Young's fringes tests in two orthogonal directions on thin amorphous tungsten taken with 80 kV electron acceleration voltage and at different defoci of (**a**) 0 nm, (**b**) 150 nm, (**c**) 300 nm, and (**d**) 600 nm. The images are cropped with a factor of two and the contrast is inverted.

Downloaded from https://www.cambridge.org/core. Ulm University, on 16 Jan 2019 at 15:38:26, subject to the Cambridge Core terms of use, available at https://www.cambridge.org/core/terms.
https://doi.org/10.1017/S1431927618000223

Table 1. Reduced axial brightness of the source for different electron acceleration voltages and dose rate illuminations

	Mean signal	Acquisition time	Conversion rate	Pixel size	Illumination semi-angle distribution	Reduced axial brightness
	counts/pixel	s	counts/e$^-$	Å^2	μrad	A/(m^2 sr V)
20 kV high rate	13,500	2	12	0.16	70	$1.8 \cdot 10^8$
20 kV low rate	660	10	12	0.16	7	$1.8 \cdot 10^8$
80 kV high rate	11,000	2	15	0.01	110	$1.8 \cdot 10^8$

conditions we fit $N = 0.475$. The respective fitted illumination semi-angle distributions for the different measurement conditions are indicated in the plot of Figure 6. The error in these fits is about 10% at maximum since the shape of the fitting curve is very sensitive to the illumination semi-angle distribution while the signal-to-noise factor mainly shifts the fitting curve vertically in the plot.

We noted above that nonlinear information transfer might lead to a substantial deviation in the assessment of the information limit by the Young's fringes test, however, for the correct determination of the illumination semi-angle distribution this fact is not relevant, as the occurrence of nonlinear information transfer shifts the data points vertically in the plot, similar to the signal-to-noise factor N, while the illumination semi-angle distribution is largely determined by the shape of the fit. The vertical shift is due to the fact that, for the Young's fringes test, nonlinearities virtually are just opening up the chromatic and spatial dampening envelopes by a certain factor, up to two. However, this is an approximation, albeit a reasonable one, since we assume that the impact on both envelope functions is equal and does not change with defocus. In any case, to avoid the complexity, a suitable sample still fulfilling the linear imaging approximation is preferable.

As mentioned earlier, we can use the illumination semi-angle distribution to determine the reduced axial brightness. The remaining necessary values we can readily read from the original images of the Young's fringes test. For example, for 20 kV electron acceleration voltage at the chosen magnification, we calibrated a pixel size of (40 pm^2) and a mean conversion rate of 12 counts/e$^-$. From the image with an acquisition time of 2 s, we read a mean signal of 13,500 counts/pixel. Thus, we have a mean rate of 3,500 e$^-$/(Å^2 s) = $5.6 \cdot 10^4$ A/m^2. Together with $\pi\sigma_\alpha^2 = 1.5 \cdot 10^{-8}$ sr and the electron acceleration voltage, equation (4) results in a reduced axial brightness of $1.8 \cdot 10^8$ A/(m^2 sr V). The data for all tested conditions can be read from Table 1.

As a first observation, the reduced axial brightness is fairly constant in all measurements as is expected. The value is slightly above the $0.75 \cdot 10^8$ A/(m^2 sr V) specified by the manufacturer of the instrument. A similar value for this combination of X-FEG and monochromator is given by Tiemeijer et al. (2012*b*). The probable use of another semi-angle definition convention like α_{FWHM} does not alter the value since it should be accounted for as a prefactor in the equations. Standard textbooks also give lower values (Reimer & Kohl, 2008; Williams & Carter, 2009). More recent works give similar values for Schottky type electron sources (van Veen et al., 2001). Alas, in this work, a dedicated column was used that is not available to the common microscope operator.

For the different dose rate conditions, equation (5) holds true, since for a 20 kV electron acceleration voltage in the first case, we get a dose rate of 3,500 e$^-$/(Å^2 s) with an illumination semi-angle distribution of 70 μrad and in the second case, 34 e$^-$/(Å^2 s) with 7 μrad, thus σ_α^2. Having confirmed this, a reasonable estimate of the illumination semi-angle distribution is possible for most TEM imaging conditions.

Summary

A facile way to measure the illumination semi-angle distribution and subsequently the electron source brightness in TEM was shown. The basic principle is to evaluate the information limit via Young's fringes tests for different defoci. We found that it is not sufficient to measure just one defocused value and that it is necessary to include the higher-order geometrical aberrations, as well as the other dampening envelope functions into the fit. The measurement method is demonstrated with the help of the SALVE instrument fitted with a FEI X-FEG with a monochromator, for which a reduced axial brightness of $1.8 \cdot 10^8$ A/(m^2 sr V) was measured.

Acknowledgments. A similar method of determining the brightness from the dependence of the information limit on the defocus was presented by Peter Tiemeijer (Thermo Fisher Scientific, Eindhoven) at the SALVE workshop in 2015. The authors thank Thomas Gemming (IFW Dresden) for providing the Faraday cup, Willem Tichelaar (CEOS GmbH, Heidelberg) for the test sample, and Martin Linck, Heiko Müller, and Stephan Uhlemann (CEOS GmbH, Heidelberg), Hannes Lichte (Speziallabor Triebenberg, Dresden), as well as Peter Tiemeijer (Thermo Fisher Scientific, Eindhoven) for helpful discussions.
We acknowledge funding from the Deutsche Forschungsgemeinschaft (DFG) and the Ministerium für Wissenschaft, Forschung und Kunst Baden-Württemberg, Germany, as well as funding through DFG Schwerpunktprogramm 1569.

References

Barthel J and Thust A (2008) Quantification of the information limit of transmission electron microscopes. *Phys Rev Lett* **101**, 200801–1–4.

Erni R (2010) *Aberration-Corrected Imaging in Transmission Electron Microscopy*. London: Imperial College Press.

Frank J (1976) Determination of source size and energy spread from electron micrographs using the method of Young's fringes. *Optik* **44**, 379–391.

Hosokawa F, Suzuki M and Ibe K (1991) Determination of the effective source from its image in the backfocal plane of the objective lens. *Ultramicroscopy* **36**, 367–373.

Lichte H, Börrnert F, Lenk A, Lubk A, Röder F, Sickmann J, Sturm S, Vogel K and Wolf D (2013) Electron holography for fields in solids: Problems and progress. *Ultramicroscopy* **134**, 126–134.

Linck M, Hartel P, Uhlemann S, Kahl F, Müller H, Zach J, Haider M, Niestadt M, Bischoff M, Biskupek J, Lee Z, Lehnert T, Börrnert F and Kaiser U (2016) Chromatic aberration correction for atomic resolution TEM imaging from 80 kV to 20 kV. *Phys Rev Lett* **117**, 076101451–076101455.

Löffler KH (1964) Erzeugung freitragender Mikroobjekte durch elektronenstrahlaktivierten Kohlefolienabbau, Dissertation, Berlin.

Müller H, Uhlemann S, Hartel P and Haider M (2006) Advancing the hexapole C_s-corrector for the scanning transmission electron microscope. *Microsc Microanal* **12**, 442–455.

Reimer L and Kohl H (2008) *Transmission Electron Microscopy*, Springer Series in Optical Sciences, 5th ed. New York: Springer Science + Business Media, LLC.

Röder F, Lubk A, Wolf D and Niermann T (2014) Noise estimation for off-axis electron holography. *Ultramicroscopy* **144**, 32–42.

Downloaded from https://www.cambridge.org/core. Ulm University, on 16 Jan 2019 at 15:38:26, subject to the Cambridge Core terms of use, available at https://www.cambridge.org/core/terms. https://doi.org/10.1017/S1431927618000223

Tiemeijer PC, Bischoff M, Freitag B and Kisielowski C (2012*a*) Using a monochromator to improve the resolution in TEM to below 0.5 Å. Part I: Creating highly coherent monochromated illumination. *Ultramicroscopy* **114**, 71–81.

Tiemeijer PC, Bischoff M, Freitag B and Kisielowski C (2012*b*) Using a monochromator to improve the resolution in TEM to below 0.5 Å. Part II: Application to focal series reconstruction. *Ultramicroscopy* **118**, 35–43.

Tsuji M and St. John Manley R (1983) Determination of the illuminating angle and defocus spread in transmission electron microscopy. *J Microsc* **130**, 93–98.

Uhlemann S, Müller H, Hartel P, Zach J and Haider M (2013) Thermal magnetic field noise limits resolution in transmission electron microscopy. *Phys Rev Lett* **111**, 046101451–046101455.

van Veen AHV, Hagen CW, Barth JE and Kruit P (2001) Reduced brightness of the ZrO/W Schottky electron emitter. *J Vacuum Sci Technol B* **19**, 2038.

Williams DB and Carter CB (2009) *Transmission Electron Microscopy*, 2nd ed. New York: Springer Science + Business Media, LLC.

Zemlin F and Schiske P (1980) Measurement of the phase contrast transfer function and the cross-correlation peak using Young interference fringes. *Ultramicroscopy* **5**, 139–145.

Downloaded from https://www.cambridge.org/core. Ulm University, on 16 Jan 2019 at 15:38:26, subject to the Cambridge Core terms of use, available at https://www.cambridge.org/core/terms.
https://doi.org/10.1017/S1431927618000223